



Capacitive performance of a heteroatom-enriched activated carbon in concentrated sulfuric acid



Kun Yang^a, Liangbo Peng^a, Dong Shu^{a,b,d,*}, Cuijuan Lv^a, Chun He^{c,**}, Lu Long^a

^aSchool of Chemistry and Environment, South China Normal University, Guangzhou 510006, Guangdong, PR China

^bBase of Production, Education & Research on Energy Storage and Power Battery of Guangdong Higher Education Institutes, Guangzhou 510006, PR China

^cSchool of Environmental Science and Engineering, Sun Yat-sen University, Guangzhou 510275, PR China

^dKey Laboratory of Electrochemical Technology on Energy Storage and Power Generation of Guangdong Higher Education Institutes, South China Normal University, Guangzhou 510006, PR China

HIGHLIGHTS

- A heteroatom-enriched activated carbon (N-ASC) was prepared from PET.
- N-ASC showed an interesting electrochemical activation phenomenon.
- The maximum specific capacitance of N-ASC is 201 F g⁻¹ in 5.3 M sulfuric acid.
- N-ASC exhibits excellent long-term electrochemical stability.

ARTICLE INFO

Article history:

Received 29 November 2012

Received in revised form

19 March 2013

Accepted 25 April 2013

Available online 6 May 2013

Keywords:

Supercapacitor

Heteroatom-enriched activated carbon

UltraBattery

Electrochemical activation

Pseudocapacitance

ABSTRACT

A heteroatom-enriched activated carbon with low surface area is prepared from poly(ethyleneterephthalate) and is used as an active electrode material for supercapacitor in 1.28 g cm⁻³ H₂SO₄ solution. Thus prepared heteroatom-enriched activated carbon is characterized by nitrogen adsorption/desorption at 77 K, X-ray diffraction, scanning electron microscopy, transmission electron microscopy, and X-ray photoelectron spectroscopy. The electrochemical characterizations are performed by cyclic voltammetry and galvanostatic charge/discharge in a three-electrode system. The prepared heteroatom-enriched activated carbon shows an interesting electrochemical activation phenomenon because of which the specific capacitance is significantly increased by charge at high potentials. The activation process involves the insertion of ions into the narrow enclosed free space inside the carbon material to generate new pores. The final results show that the heteroatom-enriched activated carbon electrode has a better discharge rate capability than the commercial activated carbon (Norit AZO) over a wide range of loading current (1–20 A g⁻¹). The highest specific capacitance (201 F g⁻¹) is obtained at 5 mV s⁻¹, which is two fold greater than the one before electrochemical activation. In addition, the specific capacitance of the heteroatom-enriched activated carbon is retained approximately 92% of the initial value after 20,000 cycles, indicating its excellent cycle stability.

© 2013 Elsevier B.V. All rights reserved.

1. Introduction

Transport is one of the largest sources of human-induced greenhouse gas emissions and fossil-fuels consumption. Thus,

there is a strong push for automobiles with reduced CO₂ emissions and improved fuel economy.

Hybrid-electric vehicles (HEVs) are developed due to the environmental concerns to reduce vehicle emissions. However, energy storage in HEVs operates continuously at high-rate partial-state-of-charge (HRPSoc) mode. Therefore, batteries used in HEVs should possess improved charge acceptance as well as longer life under HRPSoc working conditions. Lead-acid batteries are the most widely used batteries in hybrid vehicles and are highly reliable and cost-effective. However, traditional valve-regulated lead-acid (VRLA) battery can't satisfy the need of HEVs as it can't deliver the

* Corresponding author. School of Chemistry and Environment, South China Normal University, Guangzhou 510006, Guangdong, PR China. Tel./fax: +86 020 39310187.

** Corresponding author.

E-mail addresses: dshu@scnu.edu.cn (D. Shu), hechun@mail.sysu.edu.cn (C. He).

required cranking current when the state-of-charge (SoC) is below 30% and can't accept charge efficiently when SoC is above 70% [1]. In addition, under HRPSoC duty, the VRLA battery suffers from a progressive build-up of 'hard' lead sulfate and is difficult to recharge. This effect can impair battery performance and reduce charge-acceptance during regenerative braking. Moreover, high-rate discharge can make sulfation layer more compact, and the problem of over-sulfation is exacerbated during prolonged parking of the vehicle.

To address above-mentioned problems, more attention has been focused on improving the cycleability of the VRLA batteries under HRPSoC duty. Some researchers [2–4] observed that high proportion of carbon added to the negative plate of lead-acid battery can suppress the sulphation phenomenon efficiently. This way the carbon in battery can form a supercapacitor built-in, which can increase the specific power of battery. At the same time, a new technology was developed by the Commonwealth Scientific and Industrial Research Organization in Australia. This new technology on battery combined an asymmetric supercapacitor (an enhanced-power negative electrode) and a lead acid battery in a single unit, creating a hybrid car battery (UltraBattery). The UltraBattery has the advantage of being long lasting, cost effective and more powerful than past technologies used in HEVs [1]. The supercapacitor, by acting as a buffer during high-rate discharge and charge, enhances the power and lifespan of the lead-acid battery. Thus, the UltraBattery in HEVs is able to deliver and absorb charge rapidly during vehicle acceleration and regenerative braking, respectively. These favorable parameters of this technology have been described in literature in detail [5,6].

One of the key issues in new hybrid technology is to select a suitable activated carbon as a capacitive electrode material. Activated carbon is known to be the most widely used double layer electrode material and it has excellent capacitive performance in dilute sulfuric acid ($0.5\text{--}2\text{ mol L}^{-1}$). However, it has also been shown that common activated carbon can be oxidized and the specific capacitance rapidly decreases when the acid concentration increases to a certain value [7]. In fact, the environment of the UltraBattery is very harsh due to concentrated sulfuric acid electrolyte (about 5.3 mol L^{-1}). Therefore, the purpose of our research was to find a suitable activated carbon with excellent electrochemical stability, highly specific capacitance, and satisfactory rate performance in concentrated sulfuric acid.

Recently, more attention has been focused on certain non-porous graphitizable carbon (so-called soft-carbon) pre-treated with alkali. These carbons, activated with alkaline solutions such as KOH and NaOH at $600\text{--}1000\text{ }^{\circ}\text{C}$, exhibit high volumetric capacitance of $20\text{--}40\text{ F cm}^{-3}$ and wide working voltage of $3\text{--}3.5\text{ V}$ in organic electrolyte. Takeuchi et al. [8,9] first reported the KOH-activated soft carbon and found an electrochemical activation phenomenon in this material. This carbon had quite a low specific capacitance at the outset due to its relatively low specific surface area. However, its capacitance increased significantly by the first charging process, and exceeded the capacitance of activated carbon. A similar electrochemical activation phenomenon was also observed for alkali-treated soft carbon by Aida et al. [10], and showed that it is applicable to the positive electrode of a hybrid electrochemical capacitor (HEC) with a combination of hard carbon as the negative electrode. The resulting advanced HEC had much higher power and energy densities than the conventional electrical double-layer capacitors (EDLCs). Recently, Ruch et al. [11] studied the mechanism of electrochemical activation by nitrogen adsorption, electrochemical dilatometry, and in situ small-angle X-ray scattering. Their results showed that KOH activated carbon had a specific capacitance of 121 F g^{-1} after electrochemical

activation and exhibited an irreversible volume expansion of 24% during activation. It has been shown that the electrochemical activation played an important role in yielding high specific capacitance, which referred to the co-intercalation of ions and solvent into electrode materials during electrochemical activation process.

Heteroatom-enriched activated carbon has been widely investigated in recent years due to the synergetic effects of electrical double-layer and Faradaic redox reaction [12–15]. It has been generally accepted that functional groups or heteroatoms such as nitrogen and oxygen, which are present on the surface of the carbon electrode material, can not only considerably enhance the capacitance through additional faradaic reactions, but also enhance the wettability between the electrode and electrolyte. In this sense, some nitrogen-rich and oxygen-rich carbons with a small specific surface area show capacitance values comparable to the best activated carbons [16–18].

Here, we report a new type of oxygen and nitrogen-enriched activated carbon that shows an interesting electrochemical activation phenomenon in concentrated sulfuric acid. The heteroatom-enriched activated carbon is prepared from homogeneous poly(ethylene terephthalate) (PET) and is modified by NaOH activation. In fact, the nitrogen heteroatoms are introduced to the carbon framework by an ammoxidation method. The electrochemical activation behavior is investigated by cyclic voltammetry (CV) using a three-electrode system and the activation mechanism is discussed in detail in this article. Heteroatom-enriched activated carbon in our study exhibits excellent capacitive performance as an electrode material in $5.3\text{ mol L}^{-1}\text{ H}_2\text{SO}_4$ solution.

2. Experimental

2.1. Materials and procedures

2.1.1. Carbonization

Homogeneous PET was used as precursor. PET was put into a horizontal furnace, pyrolyzed at $500\text{ }^{\circ}\text{C}$ for 2 h under a N_2 flow (200 mL min^{-1}). Thus prepared sample was immersed in 0.5 M HCl at room temperature for 24 h, and then the acid-treated char was thoroughly rinsed with distilled water and dried in an oven. The final product was labeled SC.

2.1.2. Activation

NaOH was mixed with SC at room temperature by a weight ratio of 3:1. After the physical mixing, the sample was activated at $850\text{ }^{\circ}\text{C}$ in a N_2 flow (200 mL min^{-1}) for 2 h. The obtained product was washed in diluted HCl, rinsed with distilled water, and dried at $100\text{ }^{\circ}\text{C}$ for 24 h. This product was named as ASC.

2.1.3. Ammoxidation

Ammoxidation of ASC was performed under NH_3 atmosphere at $350\text{ }^{\circ}\text{C}$ for 5 h. The product was named as N-ASC.

2.2. Material characterization

The specific surface area and pore size distribution of the samples were analyzed using the Brunauer–Emmet–Teller (BET, ASAP-2020, Micromeritics, USA). X-ray diffraction (XRD) analysis was carried out between 5° and 90° by using $\text{Cu-K}\alpha$ radiation on a Y-2000 X-ray generator. The morphologies of the samples were observed under a high-resolution scanning electron microscope (SEM, JSM-6380). Transmission electron microscopy (TEM) images were investigated by JEOL JSM 2010. X-ray photoelectron spectroscopy (XPS) measurements were performed with an ESCALAB 250 X-ray photoelectron spectrometer.

2.3. Electrochemical measurements

2.3.1. Preparation of working electrode

The working electrode was prepared by mixing 80 wt.% active material, 10 wt.% acetylene black, and 10 wt.% polyvinylidene fluoride. Slurry of above mixture was made using *N*-methyl-2-pyrrolidone as a solvent, then the resulting mixture was coated onto the titanium substrate with an apparent area of $1\text{ cm} \times 1\text{ cm}$ and dried under vacuum at 60°C for 12 h.

2.3.2. Electrochemical characterization

All electrochemical experiments of the working electrodes were performed in $5.3\text{ mol L}^{-1}\text{ H}_2\text{SO}_4$ solution in a three-electrode system. A $\text{Hg}/\text{Hg}_2\text{SO}_4$ electrode and a platinum plate were used as reference electrode and counter electrode, respectively. CV and galvanostatic charge/discharge (CD) tests were conducted by a CHI 660A electrochemical working station. Electrochemical impedance spectroscopy (EIS) tests were measured in the frequency range from 10^{-2} Hz to 100 kHz by an Autolab PGSTAT30. The capacitive behavior of a material was evaluated by CV and CD. The specific capacitance based on CV or CD cycling was then calculated by using the following formulas.

$$C_m(\text{CV}) = Q/m\Delta V \quad (1)$$

$$C_m(\text{CD}) = I\Delta t/m\Delta V \quad (2)$$

where C_m is the specific capacitance (F g^{-1}), Q the cathodic charge (C), m the mass of active material in the working electrode (g), ΔV the width of the potential window (V), I the discharge current (A), and Δt the discharge time (s).

3. Results and discussion

3.1. Characterization of material

Nitrogen adsorption/desorption isotherms of SC, ASC and N-ASC are shown in Fig. 1a. It is obvious that SC follows type II isotherm, typical for non-porous materials. By contrast, ASC and N-ASC show type IV character with a clear hysteresis loop in the relative pressure range of 0.4–1.0, indicating the presence of mesopores. Fig. 1b presents the distribution of pore size determined from Barrett–Joyner–Halenda (BJH) method, which is in accordance with the results of adsorption/desorption isotherms. As shown in Fig. 1b, the pore size of N-ASC is about 4 nm and similar to that of ASC. It is well known that the pore sizes in the range of 3–5 nm are required to improve the capacitance in EDLCs [19].

Textural properties of SC, ASC and N-ASC are summarized in Table 1. The results clearly show that SC has little porosity and a very low BET surface area ($2\text{ m}^2\text{ g}^{-1}$). However, after chemical activation with NaOH, the surface area increase to 127 and $104\text{ m}^2\text{ g}^{-1}$ with the total pore volume of 0.13 and $0.09\text{ cm}^3\text{ g}^{-1}$ for ASC and N-ASC, respectively. Possible reasons for the slightly lower surface areas of N-ASC may be the high density of surface functionalities blocking the pores and the carbon shrinkage that results from the ammonia treatment [20]. The mesopore percentage (ratio of mesopore volume to total pore volume) is 92% and 91% for ASC and N-ASC, respectively, indicating highly mesoporous structure.

Results of the XRD measurement for SC, ASC and N-ASC are presented in Fig. 2. All samples exhibit two broad diffraction peaks around 24° and 43° , which correspond to the (002) and (100) facets of hexagonal graphitic carbon respectively, indicating the amorphous feature of the carbon [21]. In addition, N-ASC has similar XRD results with ASC. This result indicates that the introduction of

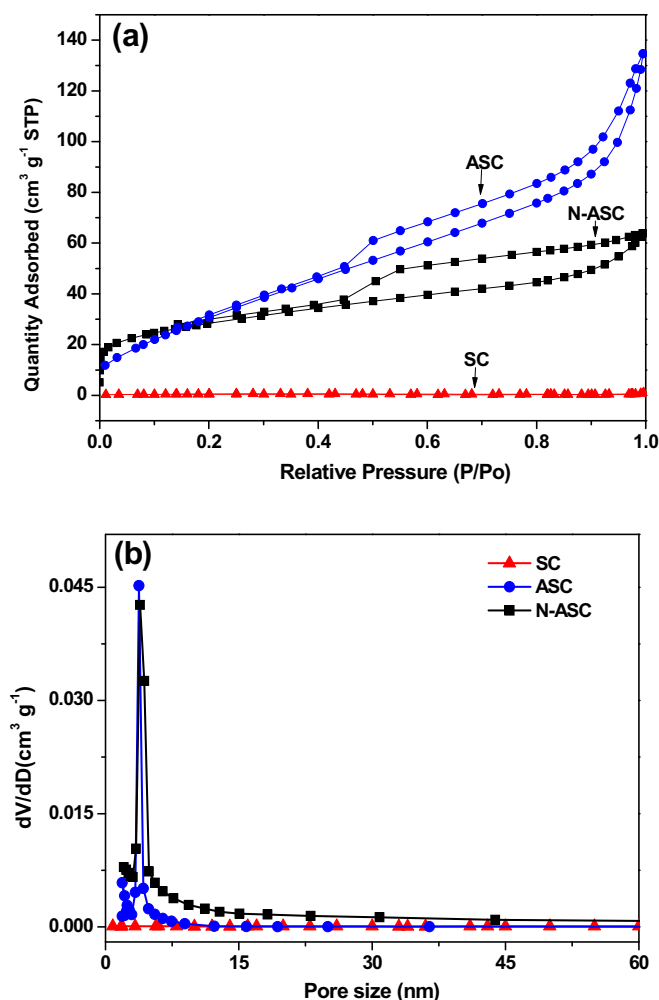


Fig. 1. (a) Nitrogen adsorption/desorption isotherms and (b) pore size distribution of samples calculated by BJH method.

nitrogen does not significantly change the crystalline structure of ASC.

Fig. 3 shows the SEM and TEM images of SC and N-ASC. It can be seen that SC (Fig. 3a) shows a rather smooth surface without pores, which is in agreement with BET results. On the other hand, N-ASC (Fig. 3b) exhibits a very rough surface with a number of large pores. The inner structure of N-ASC (Fig. 3d) viewed by TEM is also very different to SC (Fig. 3c). The TEM image of N-ASC shows that a lot of distorted small graphite-like crystallites are present in its microstructure. The result is in agreement with the above XRD analysis data and previous reports in KOH-activated soft carbons [22,23].

The elemental composition of N-ASC is confirmed by XPS (Fig. 4). The contribution of each species obtained by fitting N1s and

Table 1
Textural properties of SC, ASC and N-ASC.

	S_{BET}^a ($\text{m}^2\text{ g}^{-1}$)	V_{tot}^b ($\text{cm}^3\text{ g}^{-1}$)	V_{meso} ($\text{cm}^3\text{ g}^{-1}$)	V_{mic} ($\text{cm}^3\text{ g}^{-1}$)	V_{meso}/V_t	d_{me}^c (nm)
SC	2	N/A	N/A	N/A	N/A	N/A
ASC	127	0.137	0.126	0.011	0.92	4.1
N-ASC	104	0.091	0.082	0.008	0.91	3.6

^a Total surface area calculated using BET method.

^b Total pore volume, measured at $P/P_0 = 0.99$.

^c Mesopore diameter calculated using BJH method.

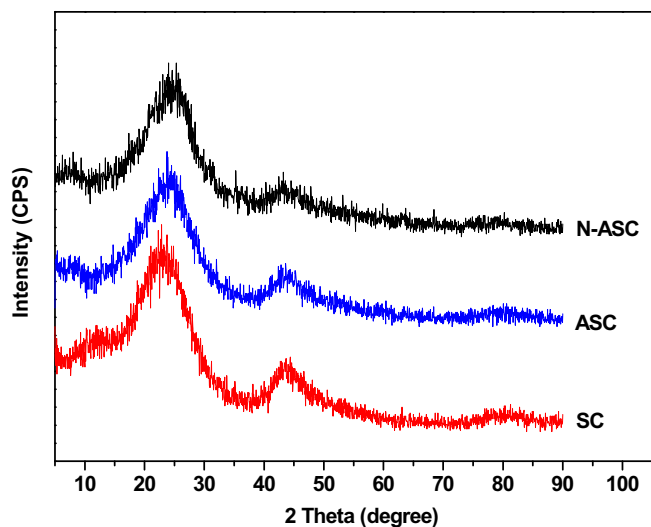


Fig. 2. XRD profile of SC, ASC and N-ASC.

O1s core level peaks are listed in Table 2. The final result shows that N-ASC consists of mainly carbon (88.2 at%), nitrogen (2.7 at%) and oxygen (9.1 at%). The fitting of the N1s peaks gives the following binding energies: 398.8 eV for N-6 (pyridinic) and imines [24]; 399.8 eV for nitrile and amide groups [25]; 400.5 eV for N-5 (pyrrolic and pyridonic) and 401.4 eV for N-Q (nitrogen substituents in aromatic graphene structures-quaternary nitrogen) [26]. It can be seen that nitrogen is present mainly in the form of N-6 and N-5 type groups (see Table 2). As report, N-6 and N-5 are usually located on the surface of the graphene layer, which can enhance hydrophilicity of the carbon materials due to their proton donor property [27]. The investigators claim that the incorporation of nitrogen after amoxidation changed the acidic–basic properties of the activated carbon that resulted in an enhanced, fast and reversible faradaic redox reaction [28]. Three types of oxygen functional groups are confirmed with the binding energies at around 532.3, 533.5 and

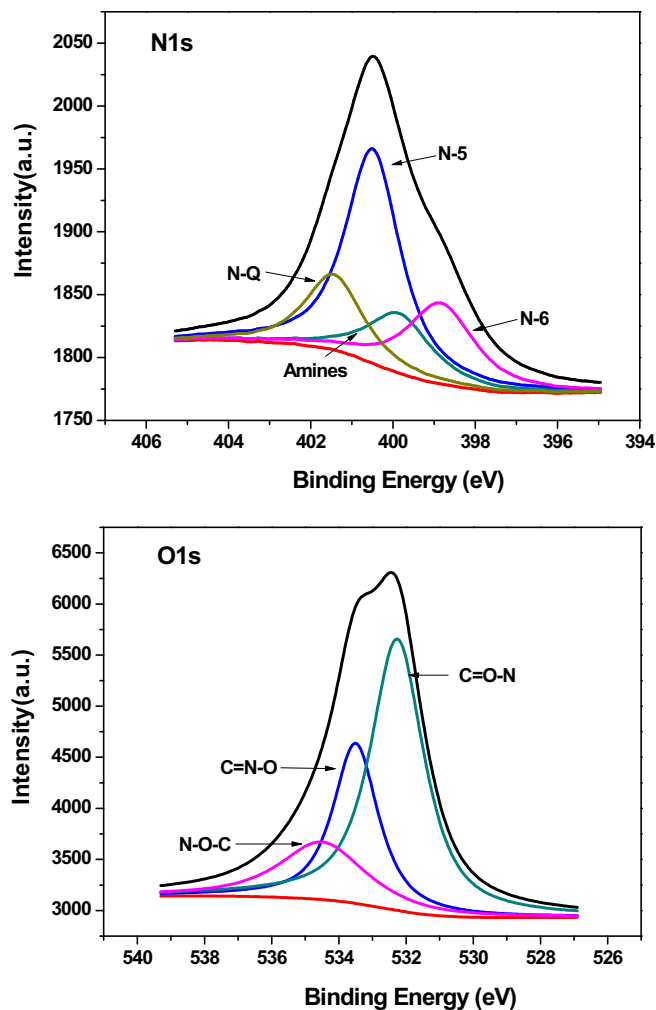


Fig. 4. N1s and O1s XPS spectra of N-ASC.

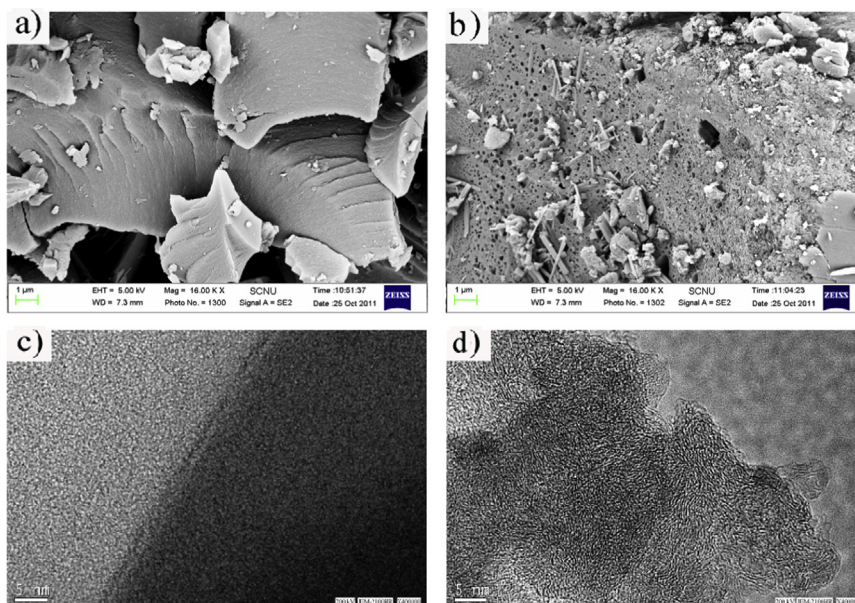


Fig. 3. SEM images of SC (a) and N-ASC (b); and TEM images of SC (c) and N-ASC (d).

Table 2

Surface composition and relative surface concentrations of nitrogen and oxygen species obtained by fitting the N1s and O1s core level XPS spectra.

Sample	Atomic conc. ^a			N1s				O1s		
	C	N	O	N-6	Amides	N-5	N-Q	C=O–N	C=N–O	N–O–C
Peak (eV)	284.8	400.4	534.2	398.8	399.8	400.5	401.4	532.3	533.5	534.3
N-ASC (at%)	88.2	2.7	9.1	21.7	15.1	46	17.2	54.7	27.1	18.2

^a C + N + O = 100%.

534.3 eV. These correspond to C=O–N groups, C=N–O and/or C–O–C groups, and N–O–C groups, respectively [29]. It can be seen that oxygen is present mainly in the form of C=O–N groups. This observation confirms the reductive role of ammonia on the oxygen-containing functionalities and thereby more nitrogen can be locked into the material through the reactions of ammonia with oxygen.

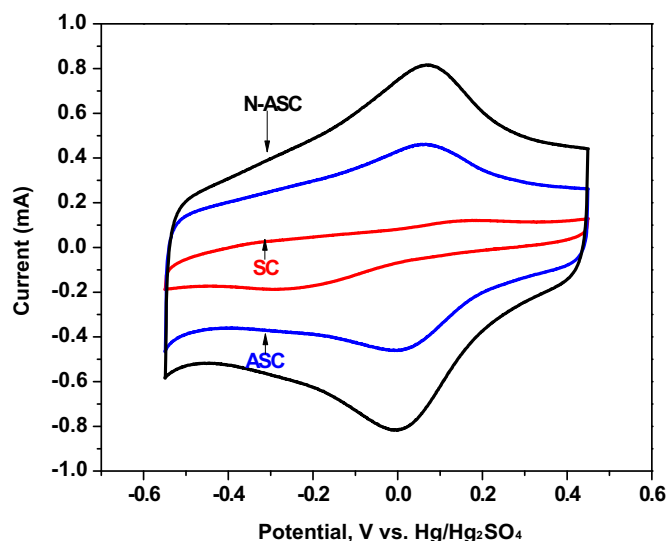
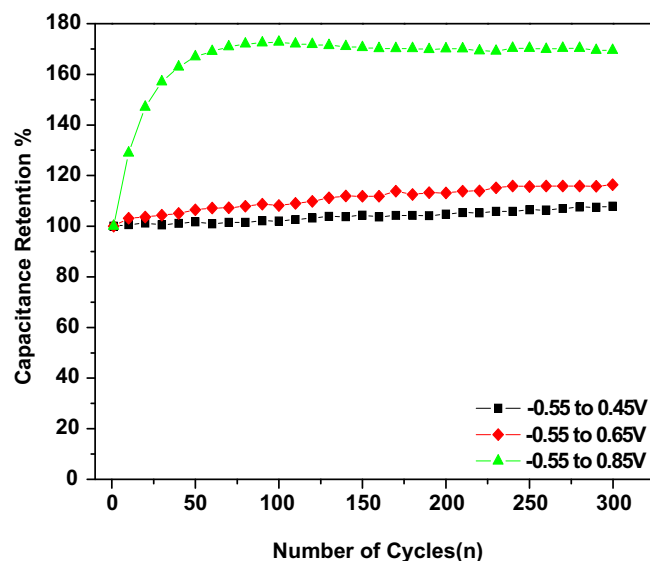
3.2. Electrochemical characterization

The first-cycle CV curve of all the samples is presented in Fig. 5. These CV curves are recorded in 5.3 M H₂SO₄ electrolyte within the potential range of –0.55 to 0.45 V versus Hg/Hg₂SO₄ at a scan rate of 5 mV s^{–1}. As shown in Fig. 5, the non-activated SC exhibits a small rectangular curve corresponding to low capacitance due to its low surface area. However, cathodic and anodic peaks are observed for both ASC and N-ASC at around 0.0 and 0.1 V versus Hg/Hg₂SO₄. These peaks are traditionally assigned to electrochemical reactions of oxygen surface functionalities such as the quinone/hydroquinone pair [30]. This result is in good agreement with the XPS study, as discussed above. In addition, the presence of nitrogen heteroatoms can considerably contribute to an additional pseudo-capacitance as well as improve the wettability on the carbon surface [16]. As shown in Fig. 5, N-ASC exhibits the highest capacitance value, in spite of smaller surface area compared to ASC. The better performance of N-ASC is obviously due to the pseudo-capacitive contribution from nitrogen groups. Similar result was also observed in low-surface-area carbon with high specific capacitance due to high nitrogen content [31]. Hence, the positive effect of ammoxidation on the capacitance characteristics of the carbon is not only connected with a change of electronic properties but certainly also with possible pseudo-faradaic reactions of the nitrogenated and oxygenated functionalities. The specific

capacitances for SC, ASC and N-ASC are calculated using equation (1) and are found to be 18, 64 and 103 F g^{–1}, respectively.

There is a very interesting phenomenon observed during CV cycling using N-ASC electrode. The specific capacitance of N-ASC is significantly increased when the electrode potential is driven beyond a threshold value. The N-ASC electrode is cycled for 300 times (5 mV s^{–1}) in different potential ranges of –0.55 to 0.45 V, –0.55 to 0.65 V and –0.55 to 0.85 V versus Hg/Hg₂SO₄. To understand the capacitance variation during the CV cycles, initial specific capacitance is set to 100%. The variation in the capacitance retention ratio as a function of cycle number is shown in Fig. 6. It is interesting to note that specific capacitance of N-ASC does not degrade but improves gradually with increase in cycle number when the positive cut-off potential is below 0.65 V. However, when the positive cut-off potential increases to 0.85 V, the specific capacitance of N-ASC rapidly increases during the initial 50 cycles and finally reaches a maximum (173% vs. the initial value) at approximately 100th-cycle and then remains almost constant for the subsequent cycles. This technique of increasing capacitance by charging the electrode to a high potential is termed as “electrochemical activation” in the present work. In fact, the electrode is badly damaged due to the electrolyte decomposition when the positive cut-off potential increases to 0.95 V. Therefore, it can be concluded that the electrochemical activation behavior of N-ASC deeply depend on the positive cut-off potential and the N-ASC electrode is successfully electrochemically activated when the positive cut-off potential is driven at 0.85 V. Thus, further experiments are performed on N-ASC electrode after electrochemical activation.

The electrochemical behavior of the N-ASC electrode after electrochemical activation is further characterized by CV. For

**Fig. 5.** CV curves of SC, ASC and N-ASC at 5 mV s^{–1}.**Fig. 6.** Variation of capacitance retention (%) with respect to cycle number at 5 mV s^{–1} in different electrode potential ranges.

comparison, the commercial activated carbon (Norit AZO), which has been studied widely in UltraBattery research, is used as a reference [4]. As shown in Fig. 7a, the CV curve of Norit shows a typical rectangular shape without any redox peaks, implying pure electric double layer capacitance. However, reversible redox peaks are observed for N-ASC after electrochemical activation. Moreover, the area of CV curve for N-ASC is apparently larger than that of Norit, suggesting a larger capacitance than latter. The specific capacitance is calculated to be 201 for N-ASC and 74 (F g^{-1}) for Norit at the same scan rate (5 mV s^{-1}). Fig. 7b shows the CV curves of N-ASC at different scan rates ranging from 5 to 100 mV s^{-1} . It can be seen that the CV curves of N-ASC are close to rectangular with a pair of redox peaks even at the high scan rate of 100 mV s^{-1} , indicating an excellent capacitive behavior and a low contact resistance of the N-ASC electrode. As a matter of fact, the specific capacitance of the N-ASC at 100 mV s^{-1} accounts for 81% of that at 5 mV s^{-1} , not much lower than 90% for the 3D carbon materials [32]. This result could be attributed to its mesoporous structure that provides the quick tunnels for the electrolyte diffusion.

Galvanostatic CD curves of the N-ASC and Norit at a high current density of 5 A g^{-1} are shown in Fig. 8a. The voltage–time curve of Norit shows ideal linear shape, while a little deviation is observed for N-ASC due to redox reactions of oxygen functional groups, consistent with the results of CV curves. In addition, the N-ASC

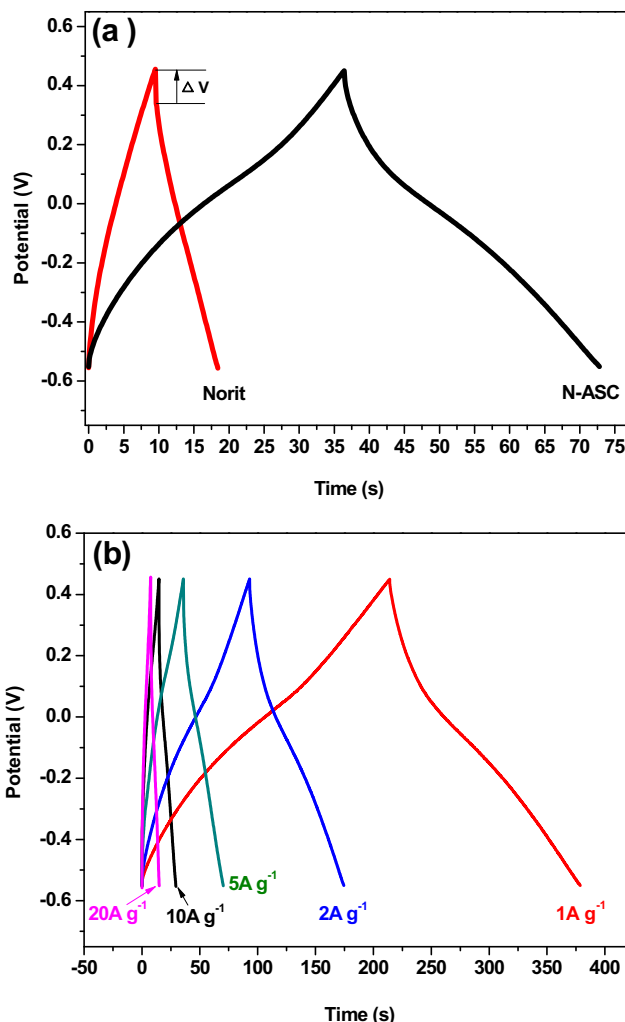


Fig. 8. (a) CD curves of N-ASC and Norit at a current density of 5 A g^{-1} . (b) CD curves for the N-ASC electrode after activation at different current densities.

electrode shows a smaller IR drop than Norit at the beginning of the discharge, indicating a rapid discharge capability and low equivalent series resistance of N-ASC. Rate capability is one of the most important factors for UltraBattery. Fig. 8b shows the CD curves of N-ASC electrode at different current densities. It shows that N-ASC possess typical triangular shapes with a little galvanostatic discharge decrease caused by the inner resistance throughout the current range of $1\text{--}20 \text{ A g}^{-1}$, indicating good capacitive properties. The average specific capacitances calculated from the CD curves at current densities of 1, 2, 5, 10 and 20 A g^{-1} are 190, 185, 178, 169 and 155 F g^{-1} , respectively. The main reason for the good performance at high CD rate may be assigned to the oxygen and nitrogen heteroatoms present on the surface of the carbon. The hydrophilic nature facilitates the penetration of aqueous electrolyte.

To understand the relationship between the specific capacitance values calculated from CV experiments and those obtained by CD tests, the scan rate in the CV experiments and the discharge time in the galvanostatic CD tests are converted into a discharge rate. The specific capacitance values of the N-ASC electrode after electrochemical activation (calculated from the CV and CD tests) versus the specific capacitance values calculated from CV experiments are slightly larger than those obtained by CD tests at the same discharge rate (Fig. 9). However, both types of values show same tendency of decreasing with the increase of the discharge rate. In

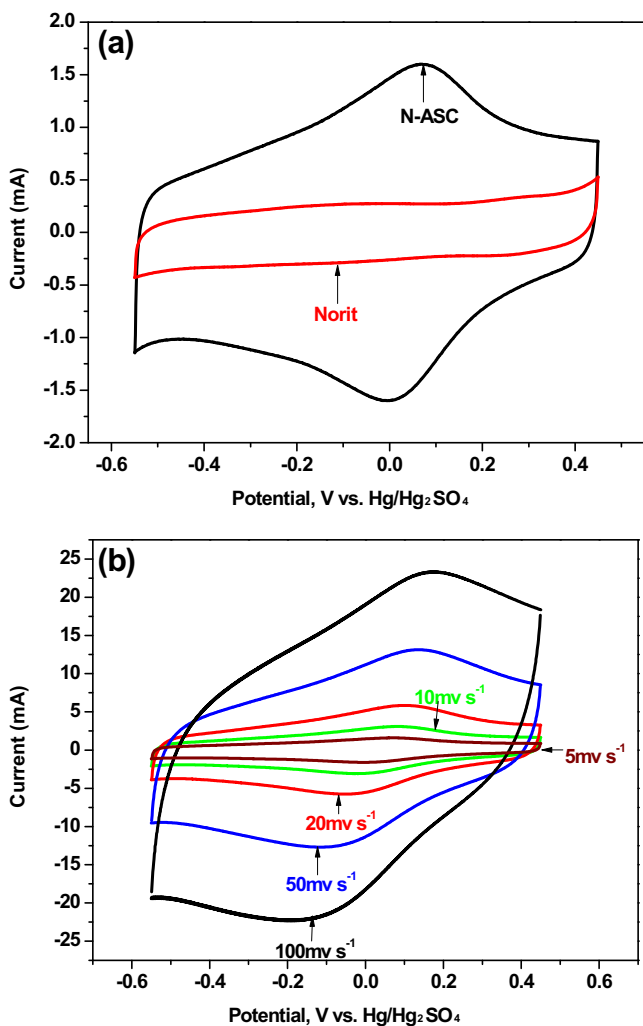


Fig. 7. (a) CV curves of Norit and N-ASC at a scan rate of 5 mV s^{-1} . (b) CV curves of N-ASC at various scan rates.

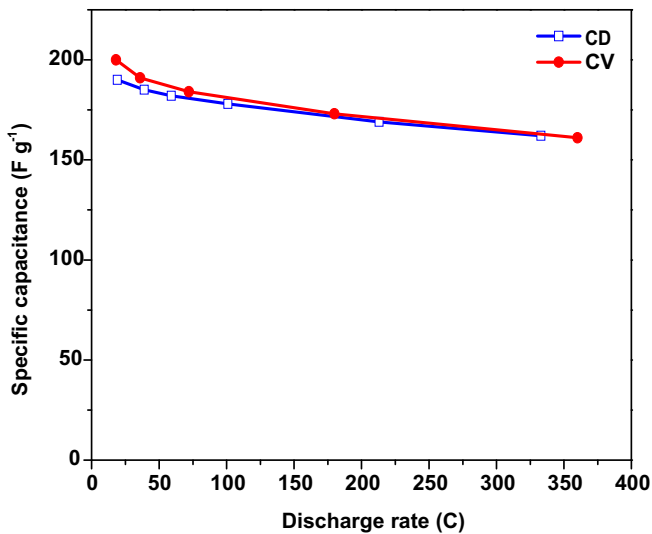


Fig. 9. The specific capacitance values of the N-ASC electrode versus the discharge rate.

general, the results suggest that the specific capacitance values calculated from CV and CD tests can be compared at the same discharge rate.

The excellent performance of N-ASC as the electrode material for supercapacitors can also be demonstrated in the Ragone plots. The energy density (E) at different average power density (P) was calculated from the CV curves at different scan rates according to the following equations:

$$E = C(\Delta V)^2/2 \quad (3)$$

$$P = E/t \quad (4)$$

where E , C , P and t are indicating of the average energy density (W h kg⁻¹), specific capacitance based on the mass of the electro-active materials in the electrodes (F g⁻¹), average power density (W kg⁻¹) and discharge time (s), respectively. Ragone plots of the N-ASC electrode at different scan rates are displayed in Fig. 10. Though the energy density of N-ASC decreases with the increase of power density, the extractable energy density of the supercapacitor

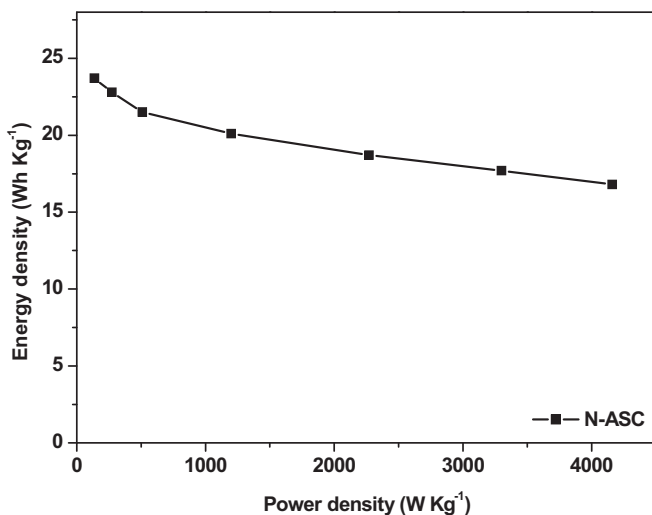


Fig. 10. Ragone plots related to energy and power densities of the N-ASC electrode.

still maintains up to 16.8 W h kg⁻¹ at the power density of 4160 W kg⁻¹, which is superior to the performance of the reported carbon materials [33].

The long-term cycling stability of N-ASC after electrochemical activation is investigated by long CV cycles up to 20,000 cycles at a scan rate of 20 mV s⁻¹ (Fig. 11a). The specific capacitance of N-ASC is almost constant during the initial 10,000 cycles and then decreases slightly upon prolonged cycling. After 20,000 cycles, the specific capacitance value remains approximately 92% of the initial capacitance value, indicating excellent cycle stability of N-ASC even at such harsh conditions. The EIS spectrums are also used to depict the difference after various cycle numbers. Fig. 11b represents the Nyquist plot obtained after the first, 10,000th and 20,000th cycles. All of the measured impedance plots are similar in shape. The semicircle in the high-frequency range is usually associated with the electrochemical processes of the N-ASC electrode, and the diameter of the semicircle corresponds to the charge-transfer resistance. As shown in Fig. 10b, the diameters of the semicircles clearly increase with increase in cycle number, indicating a worsening in the intrinsic resistance of N-ASC. However, all of the plots of the N-ASC electrode are almost perpendicular to the real axis at low frequencies, indicating ideal capacitive behavior.

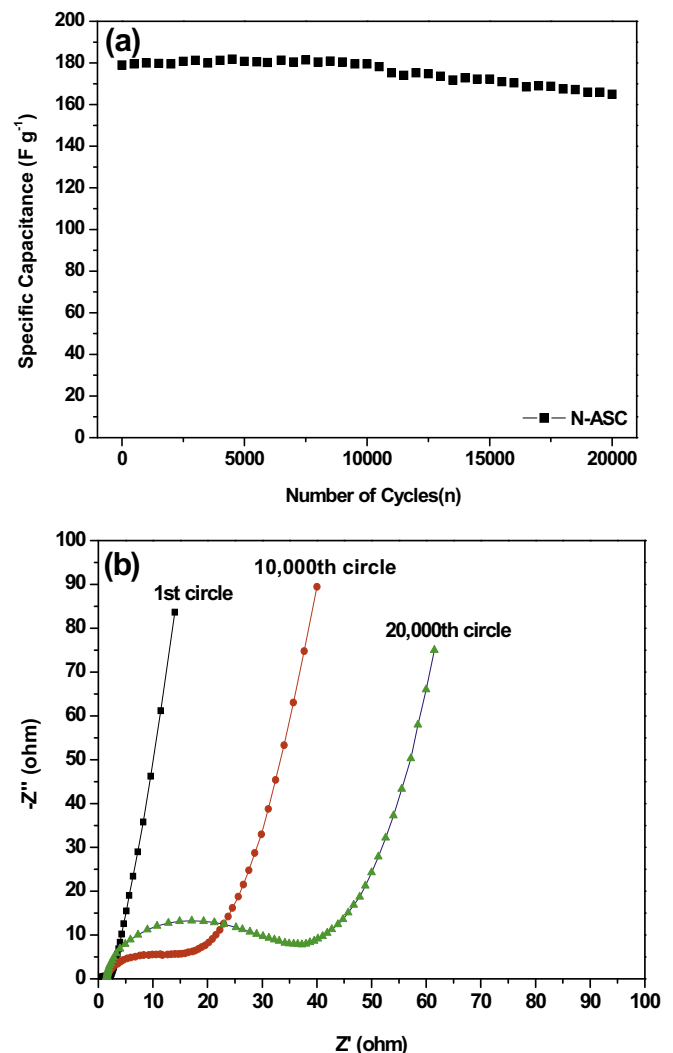


Fig. 11. (a) Variation of the specific capacitance values with the number of cycles at a scan rate of 20 mV s⁻¹. (b) Nyquist plots of N-ASC after different cycles.

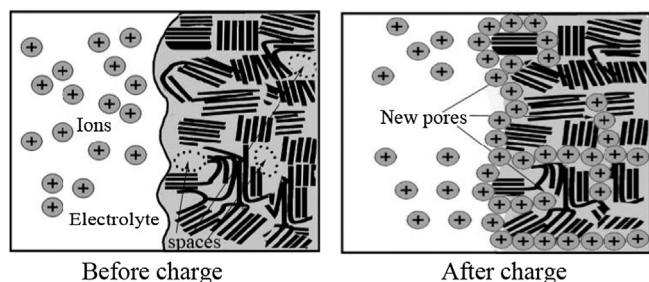


Fig. 12. Schematic of the electrochemical activation of N-ASC.

From the above results, it can be seen that the excellent capacitive performance of N-ASC could be ascribed not only to the electrochemical activation phenomena, but also to the pseudo-faradaic redox contribution involving oxygen and nitrogen functionalities. According to previous studies [8–11,34], a mechanism is proposed to explain increasing behavior of specific capacitance that is observed in the N-ASC electrode in concentrated sulfuric acid. Fig. 12 shows a schematic of the electrochemical activation process for N-ASC. As shown in Fig. 11, the N-ASC contains a large amount of distorted graphitic clusters with a lot of enclosed free spaces before charge. It is assumed that deformation of the structure is caused after charge. The smaller-sized hydrogen ions are considered to be inserted into the distorted graphitic clusters that try to invade the enclosed free spaces to form new ion-accessible pores when the electrode potential is driven beyond a threshold value. Such a structural change can be favorable to give higher capacitance by increasing the effective surface area of the electrode carbon. In our present study, we employ the fast-scan CV to investigate the electrochemical activation behavior of N-ASC because the electrode can be successfully activated electrochemically while avoiding electrolyte decomposition at such high potential. It is assumed that only a few hydrogen ions can insert into the graphitic clusters for each CV cycle. This behavior can be ascribed to fast positive-going potential sweep at high potential and less time being allowed for the ions to insert into the carbon material. Therefore, the N-ASC electrode should be cycled for hundreds of times in order to help the ions fully access into the narrow new pores. As a result, the specific capacitance of N-ASC increases significantly during the initial 100 cycles in a wide potential range of -0.55 to 0.85 V versus $\text{Hg}/\text{Hg}_2\text{SO}_4$. In addition, the structural change of N-ASC is irreversible, providing the stable capacitance and CV profile in successive runs.

4. Conclusions

In this study, a heteroatom-enriched activated carbon is prepared from PET by chemical activation with NaOH and an electrochemical activation phenomenon in H_2SO_4 solution is demonstrated. The experimental results are summarized as follows: (1) The prepared activated carbon has a low BET surface area with high oxygen and nitrogen containing functional groups. A lot of distorted graphitic clusters are present in its microstructure. (2) After electrochemical activation, the heteroatom-enriched activated carbon electrode shows a better discharge rate capability than the commercial activated carbon (Norit AZO) over a wide range of loading current (1 – 20 A g^{-1}). The highest specific capacitance (201 F g^{-1}) is obtained at a scan rate of 5 mV s^{-1} , as compared to a value of 74 F g^{-1} for Norit. In addition, the specific capacitance of the heteroatom-enriched activated carbon electrode retains approximately 92% of the initial value after 20,000 cycles, indicating good cycle stability. (3) The electrochemical activation plays

an important role in yielding high specific capacitance, which refers to the hydrogen ions inserting into the graphitic clusters and invading the enclosed free spaces to generate new pores. At the same time, the oxygen and nitrogen functional groups could not only reinforce the surface wettability of activated carbon to ensure a sufficient utilization of the exposed surface for charge accommodation but also present a high pseudo-capacitance through Faradic redox reactions. Therefore, the heteroatom-enriched activated carbon will be a promising electrode material for UltraBattery in a high concentrated sulfuric acid.

Acknowledgments

The authors wish to acknowledge the following financial supporters of this work: the National Natural Science Foundation of China (Grant No. 21273085 and 20877025), the Guangdong Province Science and Technology Bureau (Grant No. 2010B090400552), the Natural Science Foundation of Guangdong Province, China (Grant No. S2011010003416) and the Project of Guangzhou Science and Information Technology Bureau (Grant No. 2012J4300147).

References

- [1] L.T. Lam, R. Louey, J. Power Sources 158 (2006) 1140–1148.
- [2] P.T. Moseley, J. Power Sources 191 (2009) 134–138.
- [3] M. Fernandez, J. Valenciano, F. Trinidad, N. Munoz, J. Power Sources 195 (2010) 4458–4469.
- [4] D. Povlov, P. Nikolov, T. Rogachev, J. Power Sources 196 (2011) 5155–5167.
- [5] L.T. Lam, R. Louey, N.P. Haigh, O.V. Lim, D.G. Vella, C.G. Phyland, L.H. Vu, J. Furukawa, T. Takada, D. Monma, T. Kano, J. Power Sources 174 (2007) 16–29.
- [6] A. Cooper, J. Furukawa, L.T. Lam, M. Kellaway, J. Power Sources 188 (2009) 642–649.
- [7] R. Zhao, D. Shu, H. Chen, Adv. Mater. Res. 146–147 (2011) 18–21.
- [8] M. Takeuchi, K. Koike, T. Maruyama, A. Mogami, M. Okamura, Electrochemistry 66 (1998) 1311–1317.
- [9] M. Takeuchi, T. Maruyama, K. Koike, A. Mogami, T. Oyama, H. Kobayashi, Electrochemistry 69 (2001) 487–492.
- [10] T. Aida, I. Murayama, K. Yamada, M. Morita, J. Power Sources 166 (2007) 462–470.
- [11] P.W. Ruch, M. Hahn, D. Cericola, A. Menzel, R. Kotz, A. Wokaun, Carbon 48 (2010) 1880–1888.
- [12] A.D. Pasquier, A. Laforgue, P. Simon, J. Power Sources 125 (2004) 95–102.
- [13] V.R. Subramanian, S. Devan, R.E. White, J. Power Sources 135 (2004) 361–367.
- [14] T.A. Centeno, F. Stoeckli, J. Power Sources 154 (2006) 314–320.
- [15] H. Guo, Q. Gao, J. Power Sources 186 (2009) 551–556.
- [16] D. Hulicova, M. Kodama, H. Hatori, Chem. Mater. 18 (2006) 2318–2326.
- [17] E. Raymundo-Pinero, K. Kierzek, J. Machnikowski, F. Beguin, Carbon 44 (2006) 2498–2507.
- [18] G. Lota, K. Lota, E. Frackowiak, Electrochem. Commun. 9 (2007) 1828–1832.
- [19] H. Zhou, S. Zhu, M. Hibino, I. Honma, J. Power Sources 122 (2003) 219.
- [20] D. Hulicova-Jurcakova, M. Kodama, S. Shiraishi, H. Hatori, Z.H. Zhu, G.Q. Lu, Adv. Funct. Mater. 19 (2009) 1800–1809.
- [21] W.T. Huang, H. Zhang, Y.Q. Huang, W.K. Wang, S.C. Wei, Carbon 49 (2011) 838–843.
- [22] M. Okamura, M. Takeuchi, United States Patent US 6,310,762 B1, 2001.
- [23] M. Takeuchi, K. Koike, A. Mogami, T. Maruyama, United States Patent US 6,721,168 B2, 2004.
- [24] P. Burg, P. Fydrych, D. Cagniant, G. Nanse, J. Bimer, A. Jankowska, Carbon 40 (2002) 1521–1531.
- [25] J.R. Pels, F. Kapteijn, J.A. Moulijn, Q. Zhu, K.M. Thomas, Carbon 33 (1995) 1641–1653.
- [26] E. Raymundo-Pinero, D. Cazorla-Amoros, A. Linares-Solano, J. Find, U. Wild, R. Schlögl, Carbon 40 (2002) 597–608.
- [27] W. Li, D. Chen, Z. Li, Y. Shi, Y. Wan, G. Wang, Z. Jiang, D. Zhao, Carbon 45 (2007) 1757–1763.
- [28] K. Jurewicz, K. Babel, A. Ziolkowski, H. Wachowska, Electrochim. Acta 48 (2003) 1491–1498.
- [29] B. Grzyb, C. Hildenbrand, S. Berthon-Fabry, D. Begin, N. Job, A. Rigacci, P. Achard, Carbon 48 (2010) 2297–2307.
- [30] D. Hulicova-Jurcakova, M. Seredych, G.Q. Lu, T.J. Bandoz, Adv. Funct. Mater. 19 (2009) 438–447.
- [31] M. Kodama, J. Yamashita, Y. Soneda, H. Hatori, K. Kamegawa, Carbon 45 (2007) 1105–1107.
- [32] D.W. Wang, F. Li, M. Liu, G.Q. Lu, H.M. Cheng, Angew. Chem. Int. Ed. 47 (2008) 373–376.
- [33] E. Raymundo-Pinero, F. Leroux, F. Béguin, Adv. Mater. 18 (2006) 1877–1882.
- [34] S. Mitani, S.I. Lee, K. Saito, Y. Korai, I. Mochida, Electrochim. Acta 51 (2006) 5487–5493.